International Journal of Thermal Sciences 101 (2016) 35–47

Contents lists available at ScienceDirect

International Journal of Thermal Sciences

journal homepage: www.elsevier.com/locate/ijts

Contribution of convective transport to evaporation of sessile droplets: Empirical model

Florian Carle*, Sergey Semenov, Marc Medale, David Brutin

Aix Marseille Université, IUSTI UMR 7343, 13013 Marseille, France

ARTICLE INFO

Article history:
Received 23 November 2014
Received in revised form
22 September 2015
Accepted 8 October 2015
Available online xxx

Keywords:
Evaporation
Convection
Diffusion
Molecular chain
Rayleigh convection
Mass transfer

ABSTRACT

Despite the fact that sessile droplets evaporation dynamics has been studied for more than half a century, the scientific community struggles with the creation of an accurate quantitative description of the rate of evaporation. The classically used description considers evaporation as a quasi-steady process controlled by the diffusion of vapour into the air and the whole system is assumed to be isothermal at the ambient temperature. However, when two types of fluids (alcohols and alkanes) are let to evaporate on heated substrates, their evaporation rates tend to be underestimated by this model, mostly due to convection. This experimental study aims to understand how atmospheric convective transport in the vapour phase influences evaporation in order to develop an empirical model that accurately describes the evaporation rate. The Rayleigh number is used to analyse the contribution of natural convection and an empirical model is developed combining diffusive and convective transport for each type of fluid. The influence of the molecular chain length (and the increasing number of carbon atoms) is also being discussed.

1. Introduction

Sessile droplets are commonly encountered in daily life, including coffee spills [1], rain on a waterproof raincoat [2], and water falling onto a cooking plate [3]. Thanks to their ubiquity, research about sessile droplets has been conducted for centuries, and the phenomena that affect droplets, such as evaporation, diffusion and fluid mechanics, were studied even earlier. Their intensive use in various scientific and industrial applications (combustion, medicine, chemistry or again environmental processes) raised the need to predict the evaporation time which arose and became one of the main goals of droplets research field. Estimating the evaporation rate can lead to the time of evaporation and the quantity of vapour produced by a droplet. This knowledge is highly valuable for several applications especially in the field of combustion in which fuel is sprayed into a combustion chamber in the form of spherical droplets [4]. Moreover, knowing the evaporation time can allow to easily describe the droplets interface motion as the evaporation occurs [5].

The evaporation flux rate is strongly conditioned by the molecular exchange at the droplet-vapour interface and the diffusion of the vapour through the air: if molecules stay around the droplets and only move by diffusion, the air around the droplet will become saturated earlier than if molecules are carried away by an air flow. The concentration gradient between the apex *i.e.* the top of the droplet, and the air far from the droplet is the mechanism that drives and limits the evaporation. The hydrodynamic approach considers the evaporation rate being directly proportional to the rate of vapour diffusion since the air at the interface is assumed to be saturated with vapour. Maxwell was the first to describe the evaporation by the mean of a diffusion coefficient [6] and later, evaporation of spherical droplets has been studied with the same approach [7]. More recently, researches in the last decade dealt with the evaporation kinetics [2,8–11] and resulted in models predicting the evaporation rate of sessile droplets [12,13].

These classical descriptions consider evaporation as a quasi-steady process controlled by the diffusion of vapour into the air, and the whole system is being assumed to be isothermal at the ambient temperature. However, in the previous study [14], we have experimentally evidenced the contribution of atmospheric convective transport to the evaporation of a sessile droplet. In the case of diffusive evaporation (at ambient temperature, or on heated substrates under microgravity conditions), diffusive models accurately describe the evaporation rate. However, when convection appears in the vapour phase (substrate temperature above ambient

* Corresponding author.
E-mail address: florian.carle@etu.univ-amu.fr (F. Carle).

http://dx.doi.org/10.1016/j.ijthermalsci.2015.10.012
1290-0729/

Nomenclature

c_x	Vapour concentration, kg/m^3
C_x	Empirical coefficients
D	Diffusion coefficients, m^2/s
L_c	Capillary length, m
M_w	Molar mass, g/mol
N	Carbon number
P_{sat}	Saturated pressure, Pa
R	Initial droplet radius, m
$\widehat{R}$	Ideal gas constant, J/molK
T_{sat}	Saturated temperature, K
α	Thermal diffusivity, m^2/s
γ	surface tension, N/m
θ	Initial contact angle, °
ν	Kinematic viscosity, m^2/s
ρ	Density, kg/m^3

temperature under normal gravity conditions), all these models under-predict the evaporation rate.

Evaporating droplets under microgravity conditions enabled us to study the purely diffusive evaporation with intensive substrate heating, which is impossible under normal gravity conditions. As the buoyancy forces are strongly weakened, the convection process stops and the vapour behaviour is changed from convection rolls that renew the air around the droplet and enhanced the evaporation rate to only diffusion.

Vapour distribution around a sessile droplet have been very recently studied using experimental [15,16] and numerical [17,18] approaches in the case of purely diffusive evaporation. Kelly–Zion et al. [15] have recently shown by infrared spectroscopy and computed tomography that the vapour emitted by sessile drops at room temperature behaves differently as compared to the commonly accepted diffusion limited model. In this present article, we propose to somehow extend this study of vapour diffusion for droplets for a larger range of temperature differences and use microgravity environment to study pure diffusion vapour diffusion.

Models taking into account convection are developed in the combustion community to predict the evaporation time in order to obtain the best reagents concentration for combustion [19–21]. The most common, the Spalding evaporation model, takes into account convection with the calculation of mass and heat balance separately in each phase at the interface [22]. This model is based on numerous assumptions (isothermal spherical droplet, quasi-steady gas boundary, vapour/liquid phase equilibrium at the interface, air and vapour behave like a perfect gas, use of Fick's law of diffusion) that are similar to the purely diffusive model used in this study. This model, based on the Spalding mass number B_m, slightly over-predicts the evaporation rate of droplets evaporating under reduced gravity conditions *i.e.* for purely diffusive evaporation [14]. For this reason, the purely diffusive model has been chosen as a basis for our empirical model on.

New models that are able to correctly predict diffusive and convective evaporation are emerging [14,23] but their use is limited to peculiar fluids. Therefore, the aim of this article is to determine the limits of purely diffusive models and to develop, based on numerous experiments, an empirical model that accurately describes the evaporation rate of a sessile droplet on a heated substrate, regardless of the temperature or the type of fluid. The atmospheric contribution to a sessile droplet evaporation will also be investigated numerically.

2. Experiments

2.1. Fluids properties

For the purpose of this experimental study, two types of fluids (both linear carbon chains) have been chosen to be evaporated onto heated substrates: alcohols; from CH_3 OH (methanol) to C_7 H_{15} OH (heptanol), and alkanes; from C_5 H_{12} (pentane) to C_{10} H_{22} (decane). The fluids, obtained from Sigma Aldrich, are anhydrous with a purity of 99% or higher and contain only one compound except for hexane which is a mixture of isomers. The fluids have been used without any treatments prior to the experiments. All fluids properties can be found in Table 1. Properties are given at medium temperature $T_m = 40$ °C (unless otherwise indicated). The temperature dependences of properties have been taken into account in all calculations. Moreover, through this article, properties have been either measured in our laboratory or are extracted from literature sources.

2.2. Experimental set-up

The experimental set-up (Fig. 1), based on our previous work [28], enables the creation of droplets on a heated substrate (a range of temperatures between 20 °C, room temperature and 55 °C is investigated) and the monitoring of their evolution with a side-view CCD Camera which follows the evolution of the geometric parameters (radius, contact angle and height of the drop).

As this experimental set-up can be run either on Earth (1 g) or under reduced gravity conditions (microgravity 0.01 g, Moon gravity 0.16 g and Mars gravity 0.38 g), several modifications are brought to the experimental set up to obtain the most precise measurements in each conditions and are explicated in this section. The reduced gravity experiments take place aboard the Novespace's A300-ZeroG aircraft in Bordeaux (France). This aircraft is dedicated to parabolic flights and creates 22 s of reduced gravity framed by two stages of hypergravity (1.8 g).

In the laboratory, the droplets are created with a micro-dispenser controlled by computer above the substrate without the cell lid and are slowly deposited onto the substrate. As this method is technically very complex during reduced gravity experiment, the fluids are injected through a thin 0.7 mm pipe at the centre of the substrate with a motorized syringe-pump into an enclosed cell.

The droplets are then allowed to evaporate in an atmosphere composed of air at a temperature (T_a) of 20 ± 1 °C and a pressure (p_a) of 1 bar for laboratory experiments (the cell is open during all the droplet evaporation to insert the microdispenser) and 835 ± 2 mbar for microgravity experiments (cabin pressure during flight) in a closed configuration. The experimental conditions of the cell are recorded using a pressure sensor and a thermocouple of type K.

The substrate temperature and the heat-flux absorbed by the droplet are measured with a type-K thermocouple and with a heat flux-metre, respectively. The last one contains a large number of thermocouples connected in series and has a diameter of 15 mm and a thickness of 0.6 mm. Its copper body provides its high thermal conductivity and, consequently, its negligible thermal resistance to the heat flux from the heater (disk-shaped polyimide thermofoil heater regulated by a PT-100 sensor with a PID regulator at 0.1 °C) to the droplet.

The heat-flux metre, located between the heater and the substrate, is only used for reduced gravity experiments as they are performed into a closed chamber and the evaporation results in a slight increase of the chamber pressure, which pushes liquid back into droplet injection pipe. There is also a possibility of trapped

Table 1
Fluids properties at T = 40 °C and P = 101.325 kPa, except for P_{sat} and γ, T = 20 °C. The molar mass M_v, vapour density ρ_v, vapour viscosity ν_v, latent heat L_v, saturated temperature T_{sat} and saturated pressure P_{sat} are obtained from Ref. [25] while surface tension γ is from Ref. [26] except for heptane and decane [27]. The capillary length L_c and the contact angle θ are also provided for each fluids.

Fluids		M_v [g/mol]	ρ_v [kg/m^3]	ν_v [mm^2/s]	L_v [kJ/kg]	T_{sat} [K]	P_{sat} [kPa]	γ [mN/m]	L_c [mm]	θ [°]
Methanol	CH_4O	32	0.486	21.7	1111	333	13.80	22.5	1.70	21
Ethanol	C_2H_6O	46	0.322	28.5	857	347	5.83	22.3	1.70	20
Propanol	C_3H_8O	60	0.159	51.8	664	370	2.40	23.7	1.74	25
Butanol	$C_4H_{10}O$	74	0.082	81.3	423	390	1.17	24.6	1.78	28
Pentanol	$C_5H_{12}O$	88	0.059	119	505	411	0.20	25.6	1.81	29
Hexanol	$C_6H_{14}O$	102	0.238	27.3	486	430	0.10	24.5	1.73	36
Heptanol	$C_7H_{16}O$	116	0.010	611	440	488	0.01	26.2	1.82	37
Pentane	C_5H_{12}	72	3.37	2.17	357	309	57.90	16.0	1.65	18
Hexane	C_6H_{14}	86	1.27	5.47	335	342	17.60	18.4	1.72	20
Heptane	C_7H_{16}	100	0.48	13	317	371	5.33	19.3	1.72	21
Octane	C_8H_{18}	114	0.18	33	303	399	1.47	21.7	1.80	23
Nonane	C_9H_{20}	128	0.07	82	295	424	1.33	22.9	1.82	26
Decane	$C_{10}H_{22}$	142	0.03	208	263	447	0.19	23.9	1.85	28

bubbles in the tubing that occurs when g-jitter strongly affects the flow during some maneuvers of the flight. Both these factors result in a droplet suction back into tubing (while pressure in the chamber grows, a bubble in the tubing gets compressed and reduces its volume). Thus, the side-view CCD camera captures not only evaporative reduction of droplet's volume, but also its reduction due to liquid suction, which makes it impossible to extract the evaporation rate from visual data. Therefore both side-view camera and heat flux-metre were used for experimental measurements in reduced gravity: first one for determination of the droplets geometry, and second one for the calculation of total evaporation rate obtained from:

$$\frac{dm}{dt} = \frac{QS}{L_v} \tag{1}$$

where Q is the evaporative heat flux, S the wetted surface area and L_v the latent heat of vaporization (in J/kg). The evaporative heat flux Q is the heat-flux density obtained by the heat-flux metre minus the radiative exchange between the dry surface area obtained from the top infrared camera (the droplets are smaller than the substrate) and the cell. The error induced by this technics are taken into account by the error bars plotted on Fig. 2. More information about this technic can be found in our previous study [28]. For laboratory experiments, the camera is used to obtain the

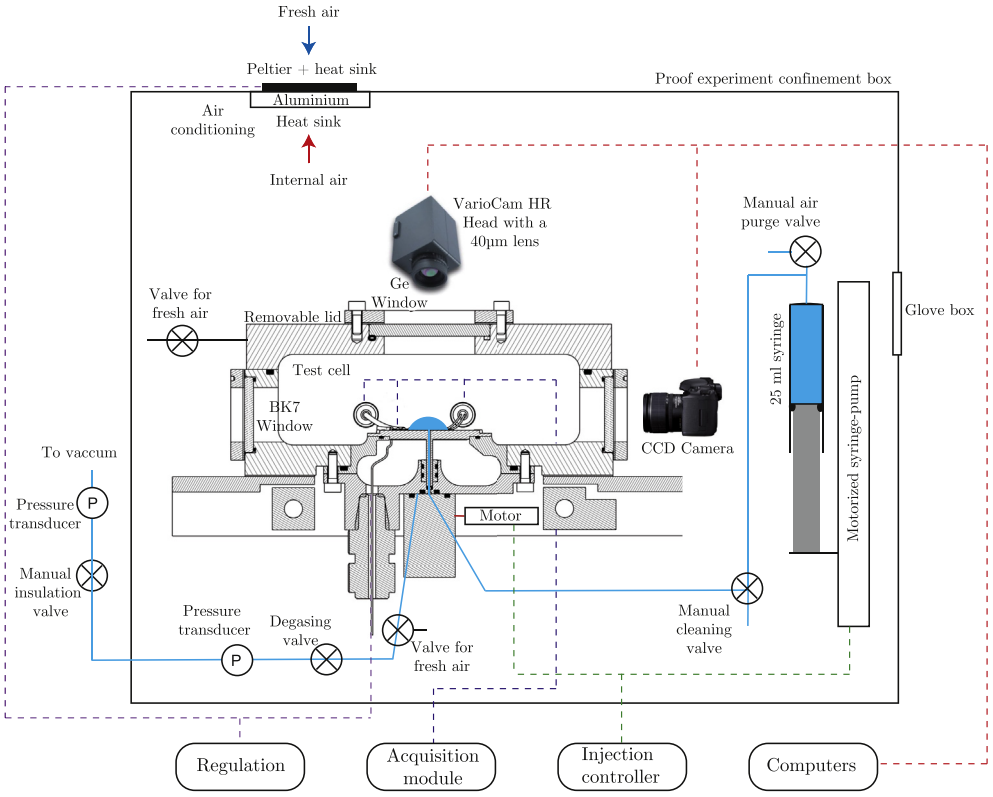

Fig. 1. Confined volume and the equipment used for the sessile droplet injection and evaporation on a Nuflon substrate: a test cell that contains a heating substrate and a heat flux-metre, a one-way syringe-pump and visible and infrared cameras. The figure shows the aircraft configuration for experiments in reduced gravity. For laboratory experiments, the injection pipe is closed, the lid is removed and a microdispenser controlled by a computer creates the droplet above the substrate and slowly deposits it onto the substrate.

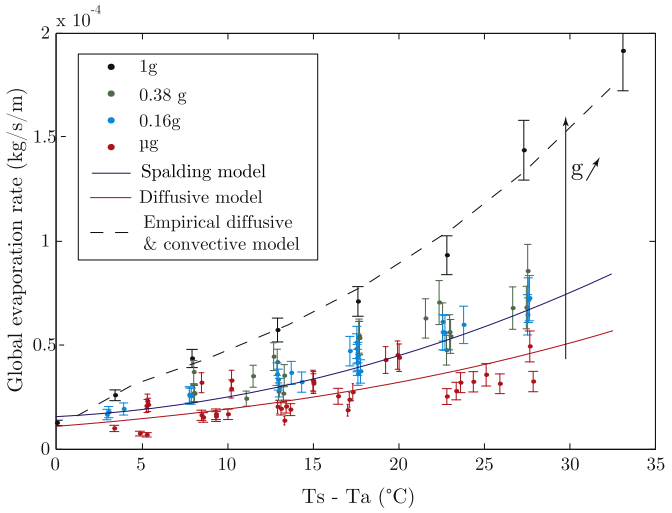

Fig. 2. Global evaporation rate of ethanol droplets under various gravity levels —Earth (1 g), Mars (0.38 g), Moon (0.16 g) and micro (10^{-2} g) gravity — as a function of the temperature difference between substrate and ambiant air (20 °C). Coloured dots are experimental data with their error bars, and lines are the Spalding model (Equation (6)), diffusive model (Equation (3)) and empirical diffusive and convective model (Equation (18)). (For interpretation of the references to colour in this figure legend, the reader is referred to the web version of this article.)

geometric parameters and the evaporation rate by image analysis (see Section 2.3).

Alcohols droplets are let to evaporated onto PFC substrates whereas alkanes droplets are deposited onto PTFE substrates (see Table 2). Substrates have been chosen for their surface energies inducing a good wetting *i.e.* low initial contact angles, and pinning of the triple line during the large part of the evaporation. However, the dissolution of the PFC substrates by alkanes forced us to use PTFE substrates instead for this type of liquid. Due to the small thickness of the substrates, their thermal conductivity difference does not influence the temperature gradient imposed by the heater and the ambient air (negligible 0.3 °C temperature decrease at the interface coating/air for a set point at 40 °C for the PTFE substrate compared to the temperature gradient between the substrate and the droplet's apex 3.51 °C in the same configuration) and therefore the evaporation rate. On theses substrates, alcohols and alkanes are fairly wetting due to their low surface tension and therefore induce small contact angles (lowest contact angle $\theta_{pentane} = 18°$, and highest contact angle $\theta_{heptanol} = 37°$).

Evaporation takes place inside a test cell, which is large enough to ensure a constant vapour concentration far from the droplet and below saturation, to prevent from any potential external. The air inside the test cell is renewed before each experiment to make sure that previous experiments do not influence the later ones. In the aircraft, after each microgravity stage, the cell is connected to the plane vent-line to flush the vapour. Once the pressure drop has vacuumed the remaining liquid, vapour free air at room temperature is injected inside the cell to start a new experiment. Air humidity (average relative humidity of 40%) is not controlled since it does not influence the evaporation of non-aqueous droplets.

During the microgravity experiments, as droplets evaporation lasts longer than the microgravity phase, we only focused and extracted data from this phase, putting aside the evaporation during the hyper gravity phases. As the transition between the hypergravity and the microgravity phases is sharp (less than 1 s) and the droplet injection takes about 5 s, the convection rolls inertia is small enough to not influence the purely diffusive evaporation (the intensity of the convection rolls decreases to 6% of its initial intensity in just 3 s and down to 1% in 5 s).

Besides the gravity level, the normal gravity experiments differ from the microgravity ones in the pressure conditions (atmospheric pressure) and wetting radii of the droplets (smaller than those used under microgravity, typically $R = 1.5 \pm 0.5$ mm, to avoid distortions due to gravity). It is assumed that these two differences do not modify the flow structure or the internal heat transfer mechanisms in the droplet. Consequently, the quantitative analysis of the gravity effect and comparison between the terrestrial and microgravity results is justified.

2.3. Image analysis

The drop is visualised with a side-view CCD camera (Stingray F-046 – resolution of 780 by 580 pixels) coupled with a microscopic lens (zoom × 6.5). Since droplets take several minutes to evaporate completely, a fairly low acquisition frequency (4 frames/sec) gives enough information for all the droplets. However, due to the strong volatility of pentane, the acquisition frequency has been raised to 20 frames/sec for this fluid. A LED wall produces collimated light to create a homogeneous background with a strong contrast on the thermal scene, allowing to reduce errors during the evolution of geometrical parameters accessible from a side view (diameter $d(t)$, contact angle $\theta(t)$, volume $V(t)$, height $h(t)$). The heat created by the light system is negligible in the evaporation process due to its low temperature compared to the substrate and its distance to the droplet. All geometrical parameters are obtained using a commercial software (Krüss Drop Shape Analysis 3).

For experiments in laboratory only, where the injection pipe is not influencing the droplet volume, the droplets' contours are fitted with a segment of a circle; and droplets' contact angles, diameters and heights are obtained by the calculation of the circular segment function. The volume is obtained by assuming a perfect axial symmetry of the droplet and by the integration of the droplet profile revolved around this axis of symmetry. In this study, droplets form spherical caps since they are all smaller than the capillary length. The evaporation rate dm/dt is then deducted from the evolution of the volume over time. Measurement errors are 5% on contact angle, 3% on radius and 10% on volume.

3. Influence of air convection in the test cell

This section is focused on the effect of air convection in the test cell on the evaporation dynamics of droplets. Pure ethanol droplets are allowed to evaporate in similar experimental (the cell under reduced gravity is closed while the cell under normal gravity is open) set-ups with various gravity levels onto heated substrates with temperatures ranging from the ambient one to +35 °C above

Table 2
Substrates properties, root-mean square roughness obtained using atomic force microscopy, surface energy measured by the Owen-Wendt method. The nano coating of PFC only change the surface energy but cannot overcome the roughness of the copper plate.

Material	Use	Thickness	Roughness	Surface energy
Perfluorocarbon (PFC)	Coated onto 0.6 mm thick copper	13.9 nm	1.75 µm	24.6 mJ/m^2
Polytetrafluoroethylene (PTFE)	Stuck onto the heater	0.5 mm	284 nm	26.9 mJ/m^2

the ambient one. The two sets of experiments were conducted under terrestrial (1 g) and reduced gravity conditions (Mars (0.38 g), Moon (0.16 g) and micro (10^{-2} g) gravity). The results of these experiments are plotted in Fig. 2, which shows the global evaporation rate plotted as a function of the temperature difference between the substrate and the ambient air for different gravity levels. The global evaporation flux is the evaporation flux rate divided by the initial radius R_0 used to compare all experimental data as this quantity is independent of the droplet size. The transition phase (*i.e.* the first seconds used for the droplet injection, see Fig. 4) is ignored from the global evaporation flux calculation as the fluid injection make the evaporation rate unsteady. Each data point is the evaporation rate given by one single droplet. The uncertainty of the measurements has been calculated as the quadratic sum of the absolute uncertainties of the parameters. The experimental data are compared to two theoretical models.

The first model (shown in red in the Fig. 2) gives the droplet evaporation rate, which, for a highly heat conductive substrate, is limited by the vapour diffusion into the atmosphere [29]. This theoretical model of quasi-steady diffusion-driven evaporation, implemented with the temperature variation, assumes an isothermal droplet at the temperature of the substrate. The rate of evaporation is then expressed by the equation below [5,12]:

$$-\frac{dm}{dt} = \pi R D \Delta\rho_v f(\theta), \tag{2}$$

where R is the radius of the droplet, D the diffusion coefficient [36] (for ethanol evaporating into air at 20 °C, its value is 1.21×10^{-5} m^2/s at 1 bar and 1.49×10^{-5} m^2/s at 0.835 bar), $\Delta\rho_v = \rho_0(T_s) - \rho_\infty$ with $\rho_0(T_s)$ the vapour concentration at the liquid–vapour interface calculated at the substrate temperature (assuming that the interface temperature is almost equal to the substrate temperature in first approximation) and ρ_∞ the vapour concentration far from the droplet, considered null because of the large characteristic length of the cell compared to the droplet characteristic length, and $f(\theta) =$

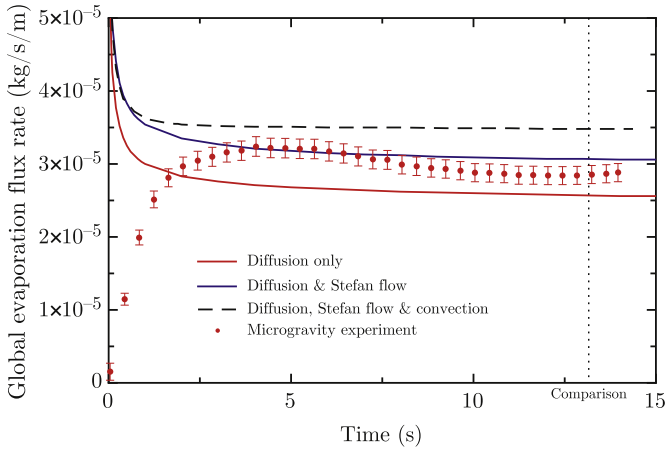

Fig. 4. Global evaporation rate over time during the evaporation of an ethanol droplet under microgravity and terrestrial gravity for a substrate temperature of 35 °C into an air at 20 °C and 835 mbar. The three plotted line are obtained from numerical simulations taking into account diffusion only (red line – microgravity), diffusion and Stefan flow (blue line – microgravity) and diffusion, Stefan flow and and natural convection (black dashed line – terrestrial gravity). The vertical black doted line represent the time chosen to compare the three models (see Equations (13) and (14)). (For interpretation of the references to colour in this figure legend, the reader is referred to the web version of this article.)

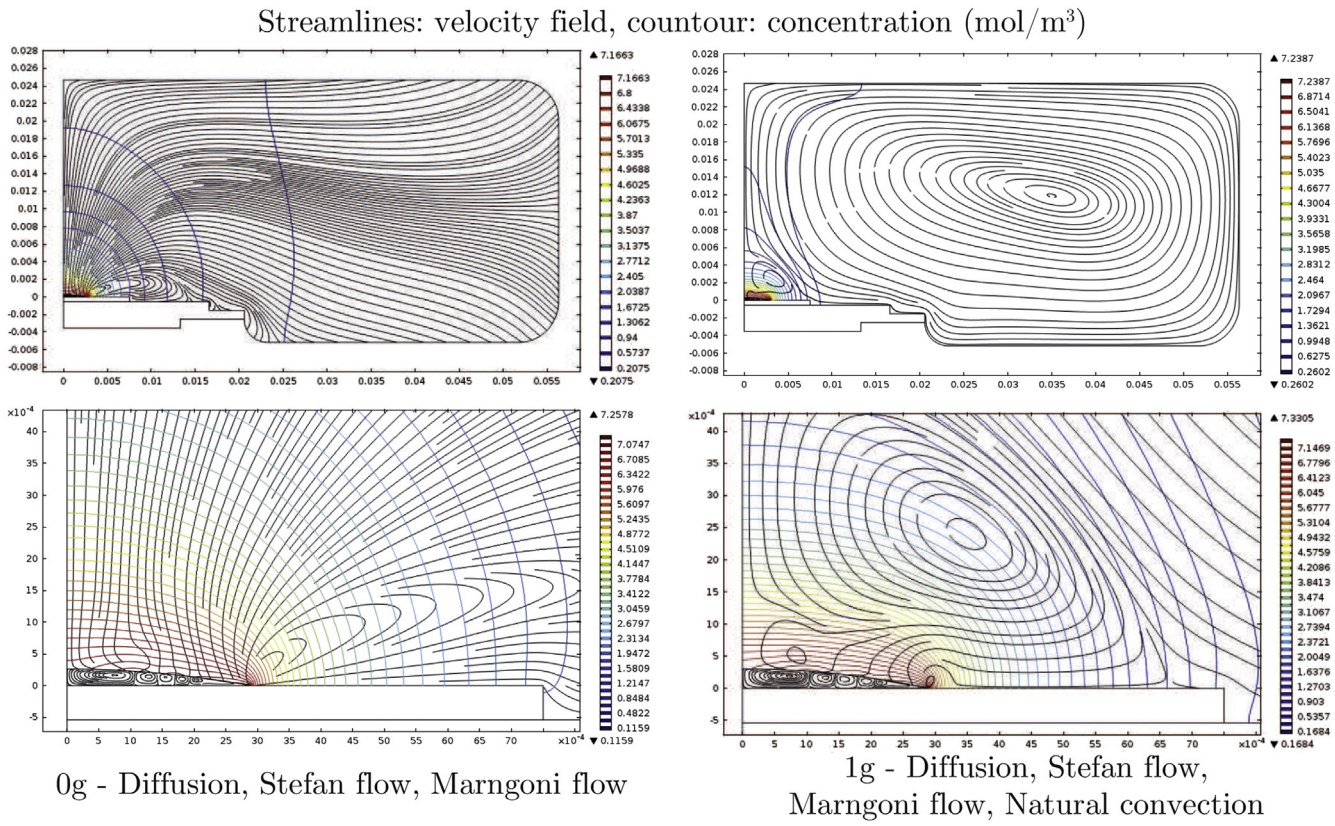

Fig. 3. Numerical simulations performed on Comsol Multiphysics of the vapour/air mixture around an evaporating droplet under reduced (left) and normal (right) gravity conditions for a substrate/air temperature difference of 15 °C. Streamlines shows velocity field and contours concentrations.

$1.3 + 0.27\ \theta^2$ is a function that depends on the contact angle, taken according to the approximation of Hu and Larson [5] (valid for angles between 0° and 90°). For angles below 40°, we note that $f(\theta)$ is almost constant at approximately 1.3 [11] (the exact theoretical value for zero contact angle is $f(0)=4/\pi$). Expression (2) is then simplified and becomes:

$$-\frac{dm}{dt} \approx 4RD\Delta\rho_v. \tag{3}$$

Equation (3) demonstrates that the evaporation rate becomes independent of the contact angle, and the radius of the droplet is the only parameter that plays a role under similar atmospheric conditions.

The density of vapour flux in the above model takes into account the diffusive term only (concentration gradient as the cause of vapour diffusion away from the droplet); it ignores the vapour/air convection and Stefan flow. Since the vapour density is lower than the liquid density, the volume of the liquid droplet is much less than the volume of the same molar quantity of vapour. Therefore, in addition to diffusion, the vapour, that is created by evaporation at the liquid–air interface, will generate a convective mass flow in the air outward from the droplet (Stefan flow) which is not taken into account by the purely diffusive models. Thus, the second theoretical model, used for the validation of our experimental data, is the Spalding model [20–22], which takes into account both the diffusion and Stefan flow. This flow can be expressed by a variant of Maxwell's equation:

$$\frac{dm}{dt} = 4\pi R^2 \left(D_v \frac{d\overline{\rho_v}}{dr} - \rho_v U \right), \tag{4}$$

$$= 4\pi R^2 \left(D_v \frac{d\overline{\rho_v}}{dr} - D_g \frac{\rho_v}{\rho_g} \frac{d\overline{\rho_g}}{dr} \right), \tag{5}$$

where $\rho_{v/g}$ are respectively the vapour and gaz (here, air) density, $\overline{\rho_{v/g}}$ is the vapour and gaz concentration respectively and U is the flow velocity. The first term inside brackets is the expression of the diffusion flux (similar to the purely diffusive model) and the second term takes into account the vapour flow. In this state, without an extensive measurement of the density gradient and the vapour velocity, the model cannot be used to compare with our experimental measurements. However, this equation can be simplified [4] by assuming that the vapour and the gas diffusive coefficients, D_v and D_g, are equal:

$$\frac{dm}{dt} = -4\pi RD(\rho_v + \rho_g) ln(1 + B_M) \tag{6}$$

$$B_M = \frac{Y_{vs} - Y_{v\infty}}{1 - Y_{vs}} \tag{7}$$

$$Y_{vs} = \left(1 + \left(\frac{p}{p_{sat}} - 1 \right) \frac{M_g}{M_v} \right)^{-1} \tag{8}$$

This model, known as the Spalding model, is based on the Spalding mass number B_M, which compares the mass fraction of vapour/gas at the droplet interface $Y_{v/g}$. $M_{g/v}$ is, respectively, the molar mass of air and vapour and p/p_{sat} is the ambient pressure and the pressure of saturated fuel vapour.

The velocity of Stefan flow at the liquid–gas interface linearly depends on the droplet diffusion limited evaporation rate due to simple boundary condition at the liquid–gas interface [24]. It means that the convective vapour flux at the liquid–gas interface is proportional to the diffusive one as evaporation is diffusion limited. Thus, taking into account Stefan flow just increases the intensity of evaporation ($\Delta\rho_v$ in Equation (3) is replaced with $\pi(\rho_v + \rho_g)$ $ln(1 + B_M)$ in Equation (6)), while its functional dependence on geometrical parameters remains the same as for pure diffusive evaporation. This allows us to apply the same geometrical factor $f(\theta)$ as in diffusive model, to the droplet's evaporation rate in the Spalding model:

$$\left(\frac{dm}{dt}\right)_{sessile} = \frac{1}{\pi}\left(\frac{dm}{dt}\right)_{spherical} \tag{9}$$

This equation is only correct if the contact angle θ is inferior to 40°, in which case $f(\theta)=4/\pi$. The evaporation rate predicted by this model is plotted in the Fig. 2 (solid blue line).

Under terrestrial gravity conditions (black dots) and at ambient temperature, the experimental value is nearly equal to the diffusive model value, consistent with other published results [2,9,11]. However, when the substrate temperature differs from the ambient temperature, the evaporation rate becomes greater than the diffusion-limited rate, and the difference between the two values increases with the substrate temperature. The first obvious observation is that the temperature strongly influences the evaporation rate: it increases with substrate temperature following the power law trend $1/R\ dm/dt = a(T_s - T_a)^b$. The discrepancy between the experimental evaporation rate and the diffusive model rapidly grows accordingly to a power law trend, and the deviation reaches up to 70% at $\Delta T = 35$ °C. Thus, this model globally under-predicts the experimental evaporation rate under normal gravity conditions. Stefan flow could explain the higher value of the evaporation rate compared to the theoretical value of purely diffusive evaporation.

As the Stefan flow is taken into account in the Spalding model (blue line), it gives estimates of the evaporation rate closer to the experimental data compared to the purely diffusive model, but it still under-predicts the observed values. The deviation between the Spalding model and the experimental data reaches 51% at $\Delta T = 30$ °C, which means that Stefan flow is not the only convective component of evaporation.

Under reduced gravity conditions (red dots), Fig. 2 shows that the diffusion-limited evaporation model correctly predicts the experimental data, despite the significant dispersion of the data due to perturbations caused by the aircraft flight. This agreement highlights that, for the first time to our knowledge, this model has been shown to be valid and can account for the variations in the substrate temperature. In the absence of gravity effects, the evaporation can then be correctly assumed being quasi-steady, diffusion-limited process, regardless of the substrate temperature and despite the assumption of an isothermal droplet. Indeed, the temperature gradient that develops inside an evaporating droplet driven by the latent heat of vaporisation appears to be negligible when the droplet is sufficiently thin and when it is evaporated on a highly heat conductive substrate [11,30,31]. In this case, the model does not need to be corrected to include Stefan flow as the evaporation rate estimation is correct. However, Stefan flow has to be taken into account in computations to have a good representation of the vapour behaviour in the cell.

Consequently, the deviation noticed under the 1 g condition can only be due to the development of another mechanism accompanying the evaporation under the influence of gravity; this additional mechanism that contributes to the diffusion increases the evaporation rate. The contribution of this mechanism is greater when the substrate temperature is higher. These observations indicate that the mechanism is the natural convection in the vapour phase that develops due to buoyant forces. Experimental evidence

can also be found in Fig. 2: despite the data dispersion, a clear increase in the global evaporation rate can be seen as the gravity level increases, indicating an increase in natural convection. We have to note that the evaporation rate measured for droplet evaporating with convection can be affected by the open cell configuration. As the cell is open to accommodate the microdispenser, the vapour can be advected by convection outside of the cell and this effect can increase the droplet evaporation rate. However, this influence is difficult to estimate in our case since non-only the configuration is modified, but the pressure is also different (824 mbar in the aircraft for μg experiments and 1 bar for experiments in the laboratory). In this article, only the global evaporation rates of droplets in the same configuration will be directly compared.

To demonstrate the effects of natural convection on the rate of droplet evaporation, we have developed a numerical model of an evaporating ethanol drop, identical to the one of our experiments. For this purpose, the commercial software COMSOL Multiphysics have been used. It applies the Final Element Method for the weak formulation of the physics equations, and all boundary conditions are applied in form of constraints with Lagrange multipliers.

One of the assumptions made is the axial symmetry of the model, which reduces the dimension of the problem down to two independent spatial coordinates (radial and vertical) and substantially speeds up the computational process as compared to a full 3D model. The origin of the cylindrical system of coordinates is located in the plane of substrate-droplet interface, and the vertical axis coincides with the axis of symmetry of the droplet. Though the real experimental cell has a square shape and not the axisymmetric one, its size is much bigger than the size of the evaporating droplet located in the cell centre. This allows us to neglect the shape and take into account only the volume of the cell. Thus in our numerical model we have created an axysimmetric cell of the same height as the experimental one, and its radius was chosen to match the experimental cell volume.

The materials parameters in the model were equivalent to the experimental ones. The air pressure inside of the experimental cell was taken as in the parabolic flight experiment and equals 824 mbar. The temperature difference between the substrate and the wall of the experimental cell was chosen to be 15.1 °C (substrate at 42.6 °C and ambient 27.5 °C) like in the particular experiment. Since the temperature change occurs mostly in the air domain (the medium with lowest heat conductivity in the system), its dynamic viscosity μ_a, heat conductivity k_a, and vapour diffusivity D_{ea} (ethanol in air) depend on local temperature: μ_a and k_a, are determined according to the Sutherland's law:

$$\mu_a = \mu_{ref}\left(\frac{T}{T_{ref}}\right)^{3/2}\frac{T_{ref}+S}{T+S} \tag{10}$$

$$k_a = k_{ref}\left(\frac{T}{T_{ref}}\right)^{3/2}\frac{T_{ref}+T_S}{T+T_S} \tag{11}$$

where $\mu_{ref} = 1.716\times10^{-5}$ Pa.s, $k_{ref} = 2.414\times10^{-2}$ W/m.K, T_{ref} and T_S respectively 273.15 and 194.4 K and S = 110.4 K. The vapour diffusion coefficient is determined according to the following formula:

$$D_{ea} = \frac{(D_{ea}\cdot p)_{ref}}{p}\left(\frac{T}{T_{ref}}\right)^{3/2} \tag{12}$$

where p is the air pressure inside the experimental cell, $(D_{ea}\cdot p)_{ref} = 1.337$ Pa.m^2/s and $T_{ref} = 298$ K [32]. As it is possible to follow the vapour during the numerical simulation, the calculations take into account the mixture of vapour/air while we use only the values of the vapour for the experimental calculations of the Rayleigh number.

As the flow velocities in the experimental cell and droplet are much lower than the speed of sound, the air and liquid were modelled as incompressible Newtonian fluids (Navier–Stokes equations). The boundary conditions at the droplet surface for Navier–Stokes equations include: the balance of normal (Laplace pressure) and tangential (thermocapillary forces) components of the full stress tensor, the continuity of the tangential component of the velocity (no-slip condition), and discontinuity of the normal component of the velocity due to evaporation process (Stefan flow). No-slip boundary condition was applied on all solid surfaces. The vapour diffusion-convection equation with temperature dependent diffusion coefficient was solved in the air domain with the boundary condition of saturated vapour concentration at the droplet surface, which in turn was also considered as a function of local droplet's temperature (Clausius–Clapeyron equation). No-penetration boundary condition was applied for the vapour at the cell walls. The equations of conductive and convective heat transfer were solved in all (solid, liquid and air) domains with boundary conditions of constant heater temperature underneath the substrate and constant ambient temperature at the walls of the experimental cell. A condition of thermal insulation was posed for the material located between the substrate and the cell wall. At the liquid–air interface a condition of the heat sink due to evaporative cooling (latent heat of evaporation) was posed as a function of local evaporation rate. The Boussinesq approximation was used in order to account for the buoyancy forces in both liquid and air domains. These forces were calculated based on the dependence of air density on temperature and vapour concentration.

As the evaporation proceeds into a closed chamber, the problem was simulated under unsteady approximation with a preheating stage followed by the establishing of the convective pattern in the air (if gravity is not zero), and finally an instant beginning of the evaporation process (droplet spreading stage is not simulated). Integration of the local evaporation rate along the droplet surface gives the total droplet's evaporation rate. Knowing this quantity at each time step, and assuming the pinning of the droplet's contact line and a spherical cap shape of the droplet, the velocity profile of the liquid–air interface was calculated and used in corresponding boundary conditions.

The left side of Fig. 3 shows the numerical results for diffusive evaporation of a droplet with Stefan flow in the air domain and Marangoni flow inside of the droplet (0 g gravity level). The right side of the figure shows the results for the same evaporation but with buoyancy effects (natural convection) taken into account in the droplet and air (1 g gravity level). The coloured contours represent the vapour concentration in mol/m^3, and the streamlines show the velocity field both in the droplet and air.

Without natural convection the air velocity around the droplet is uniform and directed outwards, except near the triple line, where the Stefan flow is strong due to the singularity of local evaporation flux. The vapour concentration is homogeneous and spherical around the droplet until it reaches the cell sides.

When natural convection takes place in the test cell, the air motion around the droplet is far more complicated than in the diffusive case. It comprises two gravitational vortices rotating in opposite directions: one is due to light heated air rising up (thermal convection) and another one is just above the droplet due descending heavy vapour (solutal convection). The vortex due to solutal convection is much smaller than the roll due to thermal convection for a $T_{sub}-T_{amb} = 15$ °C. Any further increase of the substrate temperature should enhance the influence of the thermal

vortex and therefore, solutal convection has been neglected. The empirical model will therefore neglect the solutal convection over thermal convection, as it is assumed that it is the weaker phenomenon.

Natural convection increases the mass transfer in the vapour phase, modifying the vapour field around the droplet by creating a flow and renewing the gas around the droplet. This phenomenon is clearly visible in the bottom-right picture, where a convective vortex drags the vapour away from the interface. This naturally leads to an increase of the evaporation rate, as the evaporation is controlled by the rate of vapour transport away from the droplet surface into surrounding air.

In order to quantitatively demonstrate this effect, three particular models of evaporation have been numerically investigated: 1) pure diffusive model, when neither Stefan flow nor natural convection in the air is taken into account (referred below with a subscript *diff*); 2) diffusion with Stefan flow only (referred below with a subscript $diff+S$); and 3) diffusion with both Stefan flow and natural convection accounted (referred below with a subscript $diff+S+nc$).

Fig. 4 shows the comparison between experiment and numerical simulation over time during the evaporation of a droplet for $T_{sub}-T_{amb}=15$ °C. The experimental and numerical curves behave differently at the beginning of evaporation (first 3 s) due to different initial conditions. In real experiments there is a stage of droplet injection and spreading (evaporation rate increases gradually as droplet is injected into chamber); whereas numerical model does not consider the injection/spreading stage (contact line is pinned) and evaporation starts instantaneously.

Since the evaporation process is unsteady, we have chosen one specific time moment ($t=13$ s, doted line on Fig. 4) for all three models to compare the droplets evaporation rates. The results give the following relations (substrate temperature is 15.1 °C above the ambient temperature):

$$\frac{\left(\frac{dm}{dt}\right)_{diff+S}}{\left(\frac{dm}{dt}\right)_{diff}} = 1.194 \tag{13}$$

$$\frac{\left(\frac{dm}{dt}\right)_{diff+S+nc}}{\left(\frac{dm}{dt}\right)_{diff}} = 1.355 \tag{14}$$

Since the purely diffusion-limited evaporation model does not take into account the natural convection, it obviously underestimates the experimental evaporation rate. However, it correctly describes the evaporation rate under microgravity, so the diffusive model can be used as a basis for the development of an empirical mathematical model that takes natural convection into account.

4. Influence of the molecular chain length

Once all of the fluids were evaporated at temperatures from ambient to +35 °C above ambient under normal gravity, the evaporation flux rate was measured for each case and divided by the initial radius R_0 to compare all experimental data. Fig. 5 shows the global evaporation rate as a function of the number of carbon atoms in molecular chains of different liquids for various temperatures. The evaporation rate decreases as the length of the molecular chain increases. This observation is valid for alcohols and alkanes and, to some extent, for all temperatures.

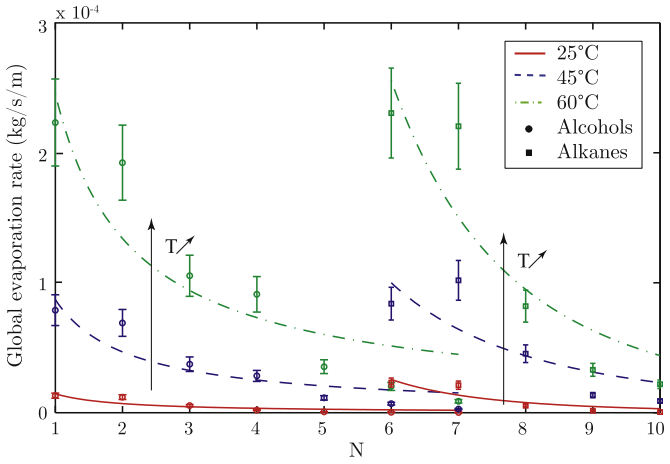

Fig. 5. Chain length dependence of the evaporation rate for alcohols (circles) and alkanes (square) at 25, 45 and 60 °C in an ambient air at 20 °C where N is the number of carbon atoms in the molecular chain. The lines fitting the data follow the power law ax^b.

It is well known that most of the evaporation occurs at the triple line for sessile droplets with low contact angles [5]. If hemispheric droplets —$\theta=90°$— have a uniform evaporation flux profile along the interface, droplets with small contact angles —$\theta<40°$— present a singularity in the evaporation flux profile near the contact line. But regardless the distribution of the evaporation flux along the droplet surface, the evaporation rate is always proportional to the droplet radius in the case of the diffusion-limited evaporation (Equation (2)). Thus the evaporation flux rates of droplets with various radii can be compared by dividing these values by the initial radiust. This is equally true for evaporation with convection in the vapour phase as the vapour motion around the droplets does not influence the evaporation process but its rate.

Longer molecular chains have less freedom and tend to entangle more easily [34]. These phenomena modify the fluids physical properties, such as density and vapour viscosity (Table 1). Indeed, the increasing vapour viscosity with the length of the molecular chain will decrease the vapour diffusion around the droplet and thereby reducing the evaporation, as diffusion is the limiting phenomenon. Moreover, the saturated pressure of the fluids decreases with the chain length increase (three orders of magnitude between methanol and heptanol) which significantly reduce the evaporation rate. The empirical model needs to take into account theses changes in fluid properties.

5. Development of the empirical model

Figs. 6 and 7 provide a closer look at each individual fluid. The global evaporation rate is plotted as a function of the temperature between the substrate and the ambient air. The error bars on the experimental data have been calculated as the quadratic sum of all of the measurement errors. All experiments can actually be considered quasi-steady because the calculated diffusion time is smaller than the measured evaporation time, $t_D/t_e=L^2/\alpha t_e\approx 10^{-3}-10^{-4}$. Plain colour lines plotted in the figure represent estimates of the global evaporation rate by the model quasi-steady diffusion-limited evaporation. In the case of sessile droplets with contact angles below 40°, the evaporation rate can be estimated by Equation (3). This diffusion-driven evaporation model implemented with substrate temperature assumes that the droplets are isothermal at the substrate temperature. This assumption can be easily justified because the temperature gradient that

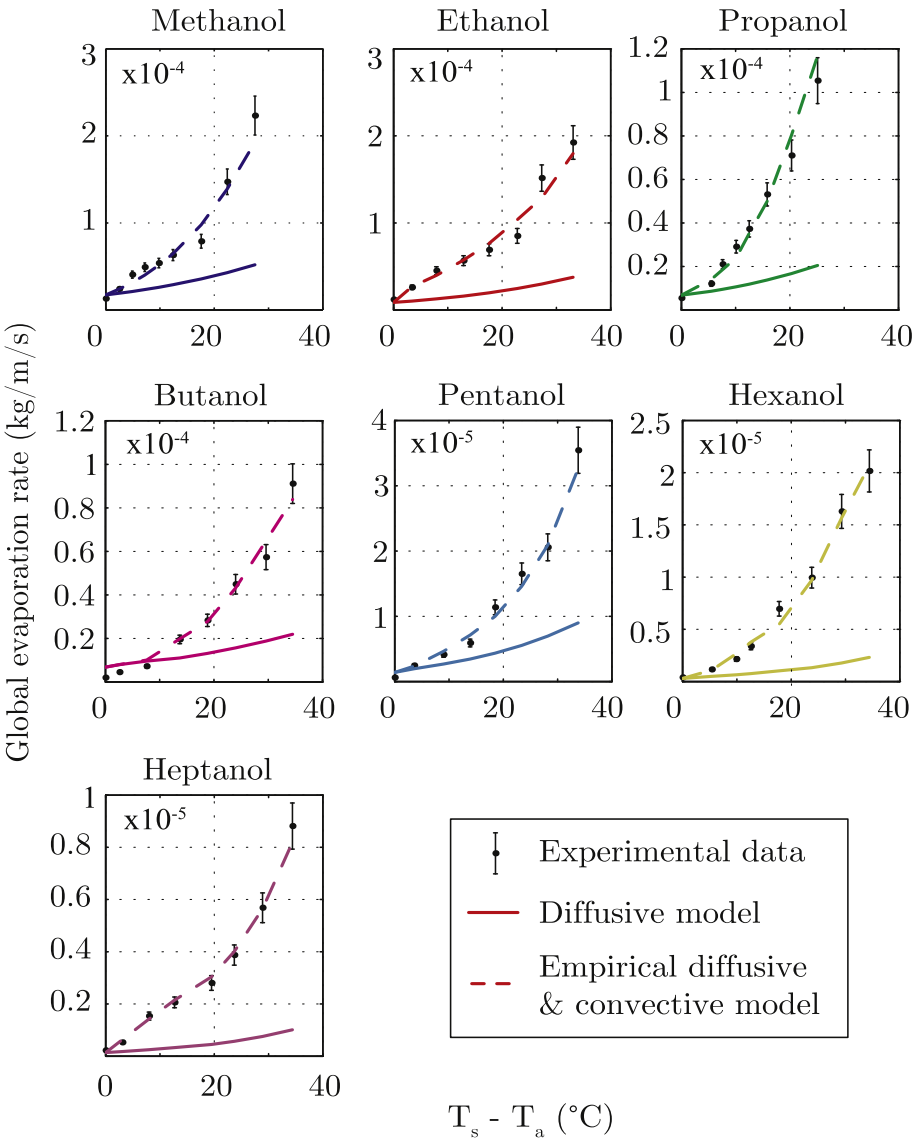

Fig. 6. Global evaporation rates of alcohols droplets as a function of temperature difference between ambient air at 20 °C and substrate under normal gravity.

develops inside the droplet, which is driven by the latent heat of vaporisation, can be neglected if the droplet is thin and evaporates on a highly heat conductive substrate, such as a thick aluminium heater with thin substrates [31].

At ambient temperature, the diffusive model is in good agreement with the experimental data (black dots), but at higher temperatures, the model under-predicts the evaporation rate with deviations of up to 100% at +35 °C. The models ability to correctly describe the evaporation process is questionable when thermal effects related to evaporation are no longer negligible, *i.e.* when the substrate plays the role of a thermal insulator [29,30,11] or when it is heated. In such cases, the deviation has been shown to result from atmospheric convection around the thermal scene [14]. Air, heated by the dry side of the substrate, rises due to buoyancy forces and modifies the concentration gradient that drives the evaporation.

Both diffusion and convection are significant in our problem. Since the diffusive and convective fluxes are locally additive [23], the evaporation rate E can be expressed as the sum of diffusive evaporation E_d, described by Equation (3), and convective evaporation, E_c, obtained experimentally thanks to droplets evaporation with the ratio E_c/E_d. Therefore, the dimensionless evaporation rate can be defined as follows:

$$E = E_d + E_c \tag{15}$$

$$E^* = E/E_d = 1 + E_C^* \tag{16}$$

where E_C^* is the dimensionless evaporation rate due to convection.

In a previous study [14], the Grashoff number was used to describe the evaporation of ethanol droplets. In this study however, this approach has been expended to several alcohols and alkanes, and in order to take into account these types, the Prandtl number must be used. Thus, the Rayleigh number, which is the product of the Grashoff number by the Prandtl number, have been implemented into the empirical model.

For dimensionless evaporation rate due to convection part, the Rayleigh number, which relates the thermal diffusivity and the convective heat transfer due to buoyancy, is used to describe the convective contribution to evaporation:

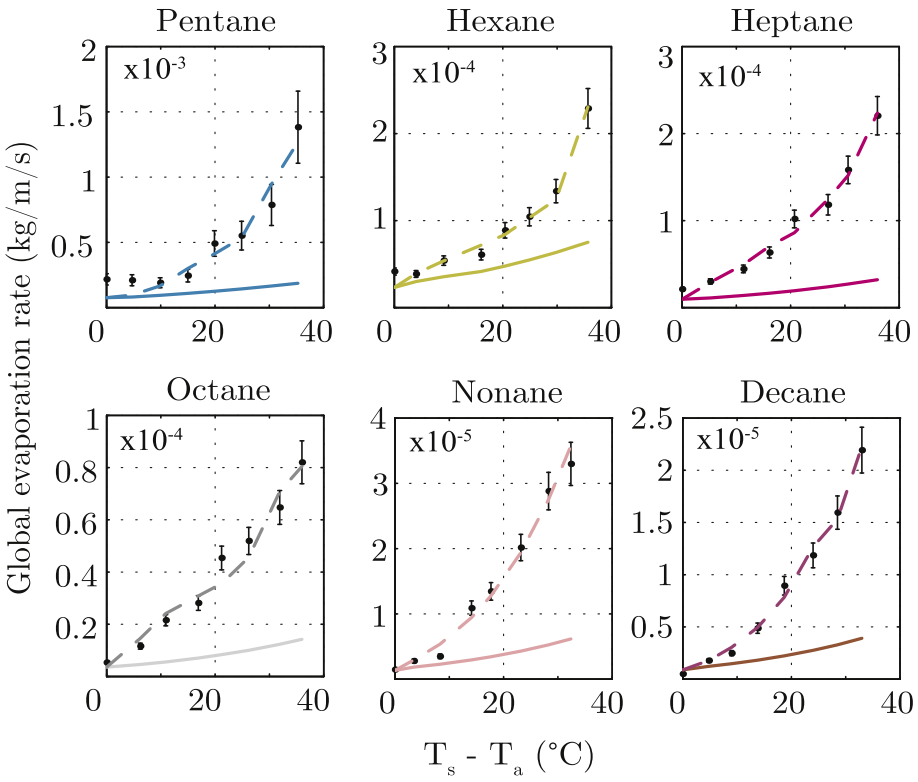

Fig. 7. Global evaporation rates of alkanes droplets as a function of temperature difference between ambient air at 20 °C and substrate under normal gravity. The legend is the same as in Fig. 6.

$$Ra = g\beta_T \Delta T R^3 \Big/ (\nu_v \alpha) \text{ with } \beta_T = 1/\rho_v \partial\rho_v/\partial T \tag{17}$$

where g is the gravitational constant, β_T the thermal expansion coefficient, ΔT the difference of temperature between the substrate and the ambient air, R the droplet radius, ν_v the vapour viscosity, α the thermal diffusivity and ρ_v the vapour density. All the variables for the Rayleigh calculations are the physical properties of the droplets vapour.

As evidenced by experiments and numerical simulations, convection acts both in the liquid (driven by Stephan flow, Marangoni flow and buoyancy forces) and the vapour phase (driven by Stephan flow as well and by solutal and thermal gradients which magnitude depends on experimental conditions such as vapour concentration and temperature difference between the substrate and the ambient air respectively). The characteristic length to describe the convection in the two phases is different: for convection in the liquid phase, the characteristic length is the droplet radius whereas in the vapour phase it is the height of the chamber. In this study, the characteristic length has been arbitrarily chosen to be the droplet radius as reference length to determine the empirical law that accounts for convection in both liquid and vapour phases.

Fig. 8 shows the dimensionless convective evaporation rate E_C^* as a function of the Rayleigh number for the two types of fluid. The Rayleigh number ranges from less than 1 for heptanol to 23,000 for pentane. This figure first shows that the convective regime of each compound vapour is laminar. To get a sense of the order of magnitude, the critical Rayleigh number for a turbulent convective air flow induced by a heated horizontal plate is $Ra_c \approx 2 \times 10^7$ [35]. In the case of short molecules, the motion of the vapour around the droplet is far from being purely diffusive (Ra > 200 for alcohols and Ra > 1500 for alkanes), and convection induces a strong concentration gradient between the droplet interface and the surrounding air. For the longest molecular chains, the Rayleigh numbers are low —less than 1, but there is still a significant discrepancy between the purely diffusive model and the global evaporation rate (6).

In a general way, the Rayleigh number decreases with the number of carbon atoms, N, in the chain while the dimensionless evaporation term E_C^* increases.

To integrate the convective part into the model, each set of data was fitted with a power law —$E_C^* = C_1 Ra^{C_2}$— giving a pair of coefficients C_1 and C_2 per fluid (Table 3). Both coefficients, C_1 and C_2, have been plotted as a function of the molar mass in Fig. 9. These coefficients only depend on the physical properties because no other experimental parameters have been changed.

The first coefficient, C_1, strongly increases with the number of carbon atoms for both types of fluids. This coefficient was fitted by an exponential law —$a.exp^{bx}$ (black line).

In contrast, the coefficient C_2 undergoes a lesser variation for all the fluid, with an average value of 0.97 and a standard deviation of 0.3 for alcohols and 0.96 ± 0.47 for alkanes. For both configurations, the Rayleigh number is small enough (below 3000) to assume a linear variation with the Rayleigh number *i.e.*, C2 could be set to 1.

By integrating these coefficients into the expression of the dimensionless global evaporation rate and by using the ideal gas law, the equation of the model can be expressed as:

$$E = 4RD\rho_0\left(1 + C_1 Ra^{C_2}\right) = \frac{4RDM_w P_{sat}}{\widehat{R}T_{sat}}\left(1 + C_1\left[\frac{g\frac{\partial\rho}{\rho_v \partial T}\Delta T R^3}{\nu_v \alpha}\right]^{C_2}\right) \tag{18}$$

where M_w is the molar mass, P_{sat} is the saturated vapour pressure at the substrate temperature, the subscripts v and s stand for the vapour and the substrate, respectively, and $\widehat{R}$ is the ideal gas constant.

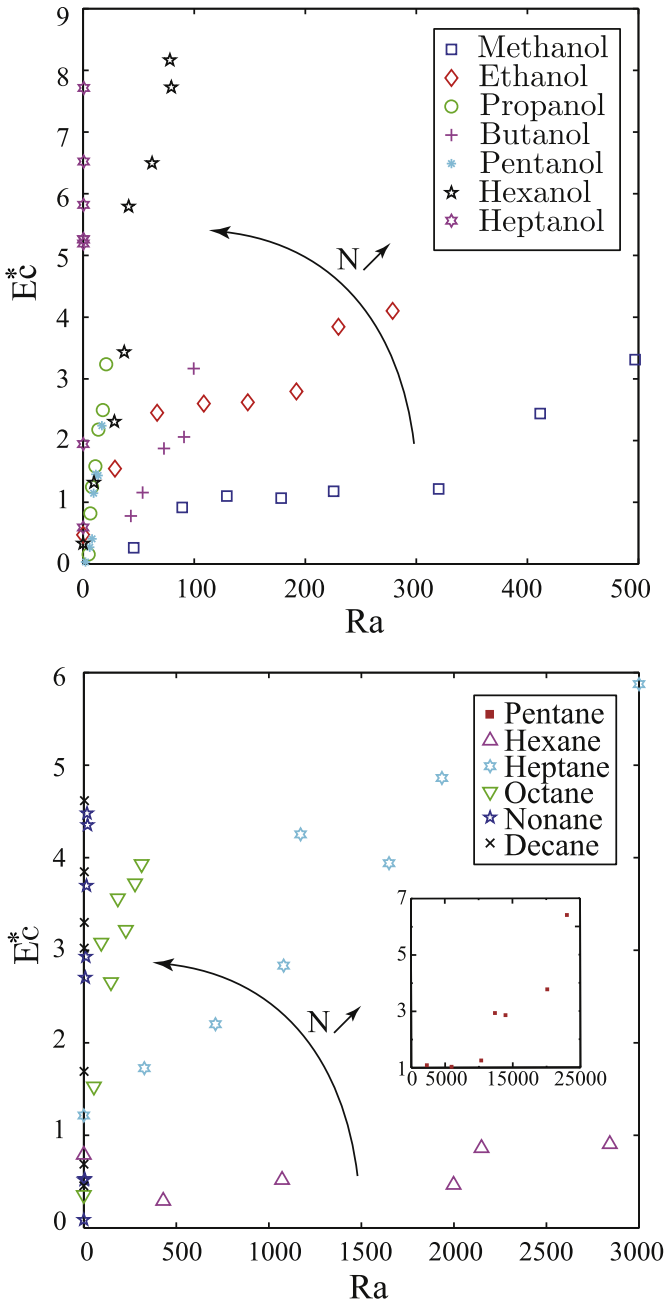

Fig. 8. Variation of the dimensionless evaporation term E_c^* as a function of the Rayleigh number for alcohols (left) and alkanes (right). The inset is a zoom out of the data for Pentane.

This empirical model is plotted in Figs. 6 and 7 using a dashed line for each fluid with their respective coefficients obtained previously.

Note that the developed model is similar to the one proposed in 2011 by Kelly–Zion et al. [23] at ambient temperature only and tested on droplets of various sizes and various liquid volatilities —3 MP, hexane, cyclohexane and heptane. The authors based their model onto the Grashof number, which compares the buoyant forces with the viscous forces. In their study, the authors also mentioned the necessity to refine their model for small droplets at ambient temperature.

6. Validation of the empirical model

A good agreement between the experimental data and the diffusive and convective models is observed. At ambient temperature, the model takes into account only the diffusive part because the temperature gradient is null. However, as soon as the substrate temperature increases, the convective part (determined by the Rayleigh number and empirical coefficients) is added to the diffusive one.

Overall, the good agreement between the model and the experimental data can be appreciated using Fig. 10, where the percentage of error, calculated by $(E-E_{exp})/E$, where E is the empirical model and E_{exp} is the measured value, is plotted as a function of the temperature difference between the substrate and the ambient air. For most of the fluids, the error is less than 10% (dashed black lines). However, one can notice larger errors at ambient and low temperatures. At these temperatures, the droplets are in a transitory phase between diffusive and convective evaporation, and the model is not accurate enough to provide a good estimation. This might also been due to the fact that only vapour convection is taken into account in the Rayleigh calculation and as the heater is bigger than the droplet, heat provided to the cell might induce a stronger convection than predicted by the calculations based on vapour only. If the ratio of vapour and air was known at each point of the cell, the ratio of the physical properties of the mixture vapour/air might be used in the Rayleigh calculation for a more accurate estimations. Moreover, our convective model does not take into account the convection induced either by the Marangoni forces in the vicinity of the droplet or the vapour diffusion. However, when the temperature increases, the average error decreases and the model can be safely used.

In order to validate this model, the empirical coefficients have been fitted —either exponential for C_1 or average for C_2— without taking into account heptanol and decane. These fits were used to determinate the coefficients for heptanol and decane (Table 4, solid markers in Fig. 9). Since the exponential fits describe the coefficients C_1 fairly well, the values for both fluids are similar. However, as the coefficient C_2 does not have a clear trend, an average value introduces some error, as can be directly observed in Fig. 11. This figure shows the global evaporation rate of heptanol and decane compared to the empirical model with the two sets of coefficients. In the case of a convective model with the coefficients from fits, it under-estimates the evaporation rate (Fig. 9, red line), primarily due to the error in the coefficient C_2. Whereas using a pair of empirical coefficients C_1 and C_2 obtained individually for each experiments, it gives a pretty good agreement (Fig. 9, black line). Refinement of the method to obtain the two coefficients is required.

Table 3
Fitting coefficients C_1 and C_2 for alcohols (top) and alkanes (bottom).

N	Alcohol	C_1	C_2
1	Methanol	5.35×10^{-3}	1.02
2	Ethanol	3.21×10^{-2}	0.90
3	Propanol	1.62×10^{-2}	1.07
4	Butanol	1.82×10^{-2}	1.07
5	Pentanol	5.79×10^{-2}	1.39
6	Hexanol	1.46×10^{-1}	0.98
7	Heptanol	9.78	0.38
N	Alkane	C_1	C_2
5	Pentane	9.29×10^{-6}	1.32
6	Hexane	5.78×10^{-3}	0.64
7	Heptane	5.38×10^{-2}	0.59
8	Octane	2.87×10^{-1}	0.46
9	Nonane	1.61×10^{-1}	1.14
10	Decane	6.19×10^{-1}	1.62

7. Conclusions

In the present article, the contribution of surrounding air convection on droplet evaporation rates was investigated both

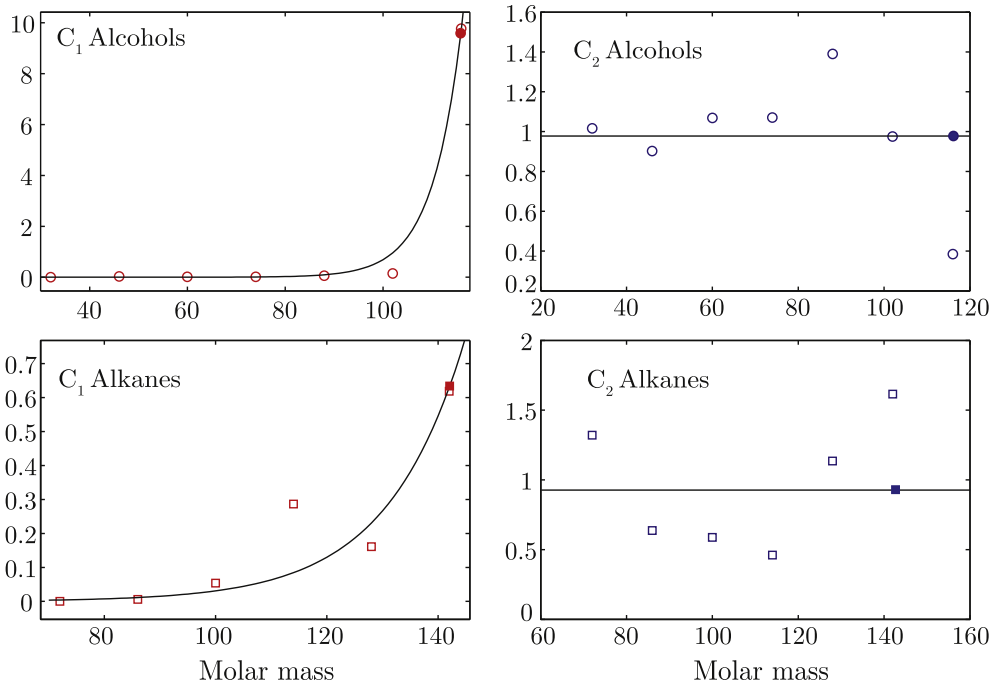

Fig. 9. Empirical coefficients C_1 and C_2 plotted as a function of the molar mass for alcohol and alkanes. Black lines are exponential fits (left) and average (right). Empty markers are the empirical coefficients while solid markers are obtained from fits or averages (Fig. 6).

experimentally and numerically during the evaporation of an ethanol sessile droplet. Although a significant discrepancy was observed between the experiments and the isothermal diffusion-driven model in usual gravity conditions, a good agreement was observed in the absence of gravity, regardless of the substrate temperature. The experimental and numerical results validate the assumptions inherent in the model under reduced gravity conditions and consequently highlight the fact that the under-prediction of this model is due to the contribution of the buoyant convection in the gas phase, which develops under the action of gravity.

To address this issue, an empirical model was developed to take into account the contribution of the atmospheric convection in the vapour phase during the evaporation of sessile droplets. This empirical model provides a good agreement with the experimental results, regardless of the substrate temperature or the fluid used. However, for temperatures near the ambient conditions, the model may require a refinement.

This study has also highlighted that the number of carbon atoms in the molecular chain and its length have a strong influence on the evaporation. To take into account this phenomenon, empirical coefficients are provided for the number of carbon atoms for both alcohols and alkanes. The strong increase of C_1 evidences the influence of the fluid properties on the vapour behaviour. However, to clarify to what extend the fluid vapour properties influence convection, a prospect experiment would be to evaporate droplets into an atmosphere of known/controlled vapour/air ratio.

For the time being, this empirical model is limited by the need to know the coefficients C_1 and C_2 for each fluid. The perspectives to improve this work would be to develop a theoretical study in order to identify the physical parameters that play a role in the coefficients values. If a direct link between the coefficients and the molecular composition is evidenced, this model could be used for any type of fluids without need to experimentally identify the coefficients. The idea is to improve this empirical model in the near future, to make it universal by accounting for as wide variety of initial conditions as possible, depending only on the molecular composition of the fluid.

The authors would like to thank CNES (Centre National d'Études Spatiales) and ESA (European Space Agency) for their financial support and the parabolic flight campaigns, as well as Novespace

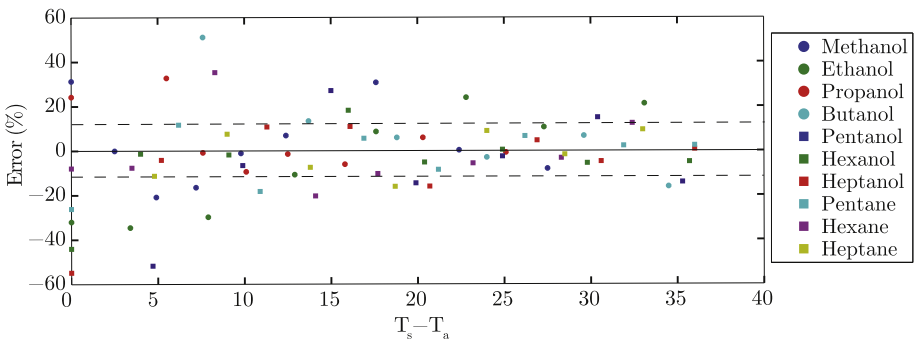

Fig. 10. Percentage of error in the model $(E-E_{exp})/E$ as a function of the temperature difference between the substrate and the ambient air.

Table 4
Coefficients for heptanol and decane obtained empirically or from the fits.

Fluids	C_1		C_2	
	Empirical	Fit	Empirical	Fit
Heptanol	9.78	9.70	0.38	0.97
Decane	0.619	0.63	1.62	0.95

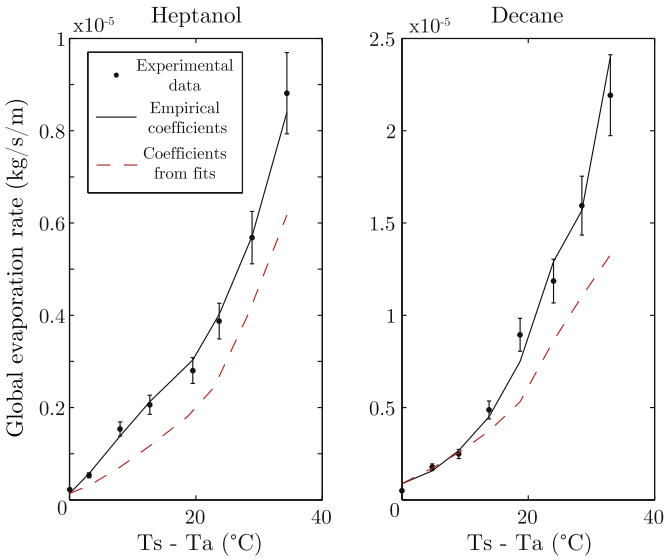

Fig. 11. Global evaporation rate of heptane and decane and the diffusive and convective model obtained from empirical coefficients (black line) and from the fits (red line). (For interpretation of the references to colour in this figure legend, the reader is referred to the web version of this article.)

for their technical support. This work has been carried out in the framework of the Labex MEC (ANR-10-LABX-0092) and of the A*MIDEX project (ANR-11-IDEX-0001-02), funded by the "Investissements d'Avenir" French Government program managed by the French National Research Agency (ANR).

References

[1] R.D. Deegan, O. Bakajin, T.F. Dupont, G. Huber, S.R. Nagel, T.A. Witten, Capillary flow as the cause of ring stains from dried liquid drops, Nature 389 (1997) 827–829.
[2] H. Gelderblom, A.G. Marín, H. Nair, A. van Houselt, L. Lefferts, J.H. Snoeijer, D. Lohse, How water droplets evaporate on a superhydrophobic substrate, Phys. Rev. E 83 (2) (2011) 026306.
[3] J.G. Leidenfrost, De aquae communis nonnullis qualitatibus tractatus, 1756. Ovenius.
[4] S. Sazhin, Modelling of heating, evaporation and ignition of fuel droplets: combined analytical, asymptotic and numerical analysis, J. Phys. Conf. Ser. 22 (1) (2005) 174.
[5] H. Hu, R.G. Larson, Evaporation of a sessile droplet on a substrate, J. Phys. Chem. B 106 (6) (2002) 1334–1344.
[6] J.C. Maxwell, S.W.D. Niven, The Scientific Papers - V2, University Press, Cambridge, 1890.
[7] I. Langmuir, The evaporation of small spheres, Phys. Rev. 12 (5) (1918) 368–370.
[8] R. Picknett, R. Bexon, The evaporation of sessile or pendant drops in still air, J. Colloid Interface Sci. 61 (2) (1977) 336–350.
[9] R. Deegan, Pattern formation in drying drops, Phys. Rev. E 61 (1) (2000) 475.
[10] S. Semenov, V.M. Starov, R.G. Rubio, M.G. Velarde, Instantaneous distribution of fluxes in the course of evaporation of sessile liquid droplets: computer simulations, Colloids Surfaces A Physicochem. Eng. Aspects 372 (1–3) (2010) 127–134.
[11] B. Sobac, D. Brutin, Triple-line behavior and wettability controlled by nano-coated substrates: influence on sessile drop evaporation, Langmuir 27 (24) (2011) 14999–15007.
[12] Y.O. Popov, Evaporative deposition patterns: spatial dimensions of the deposit, Phys. Rev. E 71 (3) (2005) 036313.
[13] H. Hu, R.G. Larson, Analysis of the microfluid flow in an evaporating sessile droplet, Langmuir 21 (2005) 3963–3971.
[14] F. Carle, B. Sobac, D. Brutin, Experimental evidence of the atmospheric convective transport contribution to sessile droplet evaporation, Appl. Phys. Lett. 102 (6) (2013) 061603–061604.
[15] P. Kelly-Zion, C. Pursell, N. Hasbamrer, B. Cardozo, K. Gaughan, K. Nickels, Vapor distribution above an evaporating sessile drop, Int. J. Heat Mass Transf. 65 (2013) 165–172.
[16] S. Dehaeck, P. Colinet, Vapour Cloud Dynamics Induced by Evaporation, arxiv, 2010, 1010.3258 [physics.flu-dyn].
[17] M. Ait Saada, S. Chikh, L. Tadrist, Evaporation of a sessile drop with pinned or receding contact line on a substrate with different thermophysical properties, Int. J. Heat Mass Transf. 58 (1–2) (2013) 197–208.
[18] Pan Zhenhai, Dash Susmita, Justin A. Weibel, Suresh V. Garimella, Assessment of water droplet evaporation mechanisms on hydrophobic and superhydrophobic substrates, Langmuir 29 (51) (2013) 15831–15841, http://dx.doi.org/10.1021/la4045286.
[19] B. Abramzon, W.A. Sirignano, Droplet vaporization model for spray combustion calculations, Int. J. Heat Mass Transf. 32 (9) (1989) 1605–1618.
[20] C. Bertoli, M. n. Migliaccio, A finite conductivity model for diesel spray evaporation computations, Int. J. Heat Fluid Flow 20 (5) (1999) 552–561.
[21] S. Sazhin, Advanced models of fuel droplet heating and evaporation, Prog. Energy Combust. Sci. 32 (2) (2006) 162–214.
[22] D.B. Spalding, The Combustion of Liquid Fuel, 1953. Pittsburgh.
[23] P. Kelly-Zion, C. Pursell, S. Vaidya, J. Batra, Evaporation of sessile drops under combined diffusion and natural convection, Colloids Surfaces A Physicochem. Eng. Aspects 381 (1–3) (2011) 31–36.
[24] S. Semenov, V. Starov, R.G. Rubio, Evaporation of pinned sessile microdroplets of water on a highly heat-conductive substrate: computer simulations, Eur. Phys. J. Special Top. 219 (2013) 143–154.
[25] NIST, Database Number 69, 2013. http://webbook.nist.gov/chemistry/.
[26] CAMEO, Database Chemicals V. 2.4.1., 2013. http://cameochemicals.noaa.gov/.
[27] L.I. Rolo, A.I. Caço, A.J. Queimada, I.M. Marrucho, J.A.P. Coutinho, Surface tension of heptane, decane, hexadecane, eicosane, and some of their binary mixtures, J. Chem. Eng. Data 47 (6) (2002) 1442–1445.
[28] F. Carle, B. Sobac, D. Brutin, Hydrothermal waves on ethanol droplets evaporating under terrestrial and reduced gravity levels, J. Fluid Mech. 712 (2012) 614–623.
[29] S. David, K. Sefiane, L. Tadrist, Experimental investigation of the effect of thermal properties of the substrate in the wetting and evaporation of sessile drops, Colloids Surfaces A Physicochem. Eng. Aspects 298 (1–2) (2007) 108–114.
[30] K. Sefiane, R. Bennacer, An expression for droplet evaporation incorporating thermal effects, J. Fluid Mech. 667 (2011) 260–271.
[31] F. Girard, M. Antoni, S. Faure, A. Steinchen, Influence of heating temperature and relative humidity in the evaporation of pinned droplets, Colloids Surfaces A Physicochem. Eng. Aspects 323 (1–3) (2008) 36–49.
[32] R. C. Reid, J. M. Prausnitz and B. E. Poling, The Properties of Gases and Liquids, United States: McGraw Hill Book Co., New York, NY.
[34] T.G. Fox, S. Loshaek, Isothermal viscosity–molecular weight dependence for long polymer chains, J. Appl. Phys. 26 (9) (1955) 1080–1082.
[35] F.P. Incropera, A.S. Lavine, D.P. DeWitt, Fundamentals of Heat and Mass Transfer, John Wiley & Sons, 2011.
[36] R.H. Perry, D.W. Green, Perry's Chemical Engineers' Handbook, McGraw-Hill, 2008.